J. Fluid Mech. (2005), *vol.* 532, *pp.* 365–388. © 2005 Cambridge University Press
doi:10.1017/S0022112005004398 Printed in the United Kingdom

Prandtl-number dependence of convection-driven dynamos in rotating spherical fluid shells

By R. SIMITEV AND F. H. BUSSE

Institute of Physics, University of Bayreuth, D-95440 Bayreuth, Germany
radostin.simitev@uni-bayreuth.de

(Received 1 June 2004 and in revised form 20 January 2005)

The value of the Prandtl number P exerts a strong influence on convection-driven dynamos in rotating spherical shells filled with electrically conducting fluids. Low Prandtl numbers promote dynamo action through the shear provided by differential rotation, while the generation of magnetic fields is more difficult to sustain in high-Prandtl-number fluids where higher values of the magnetic Prandtl number P_m are required. The magnetostrophic approximation often used in dynamo theory appears to be valid only for relatively high values of P and P_m. Dynamos with a minimum value of P_m seem to be most readily realizable in the presence of convection columns at moderately low values of P. The structure of the magnetic field varies strongly with P in that dynamos with a strong axial dipole field are found for high values of P while the energy of this component is exceeded by that of the axisymmetric toroidal field and by that of the non-axisymmetric components at low values of P. Some conclusions are discussed in relation to the problem of the generation of planetary magnetic fields by motions in their electrically conducting liquid cores.

1. Introduction

The problem of the generation of magnetic fields by motions of an electrically conducting fluid in rotating spherical shells is one of the fundamental problems of planetary and astrophysical sciences. The increasing availability in recent years of computer capacity has permitted large-scale numerical simulations of this process, but the creation of realistic models for planetary and stellar dynamos has been hampered by a lack of knowledge about appropriate external parameters. Since molecular values of material properties are usually not attainable in computer simulations because of the limited numerical resolution, eddy diffusivities must be invoked for comparisons with observations. Eddy diffusivities represent the effects of the unresolved scales of the turbulent velocity field and it is often assumed for this reason that the eddy diffusivities for velocities, temperature and magnetic fields are identical. The effects of turbulence on the diffusion of vector and scalar quantities differ, however, and large differences in the corresponding molecular diffusivities are likely to be reflected in the effective diffusivities caused by the fluctuating velocity field of the unresolved scales. In the case of the Earth's core, for example, the magnetic diffusivity is assumed to have a value of the order of $2\,\mathrm{m^2\,s^{-1}}$ (Braginsky & Roberts 1995) which exceeds the kinematic viscosity by a factor of the order 10^6. Numerical simulations are thus capable of resolving magnetic fields, but are far from resolving velocity structures. However, since the largest unresolved scales, v, l, of velocity and length yield values for an eddy viscosity $\nu_e \approx v\,l$ of the order $1\,\mathrm{m^2\,s^{-1}}$ or less, it is reasonable to assume magnetic Prandtl numbers less than unity. Since the concept of eddy

https://doi.org/10.1017/S0022112005004398 Published online by Cambridge University Press

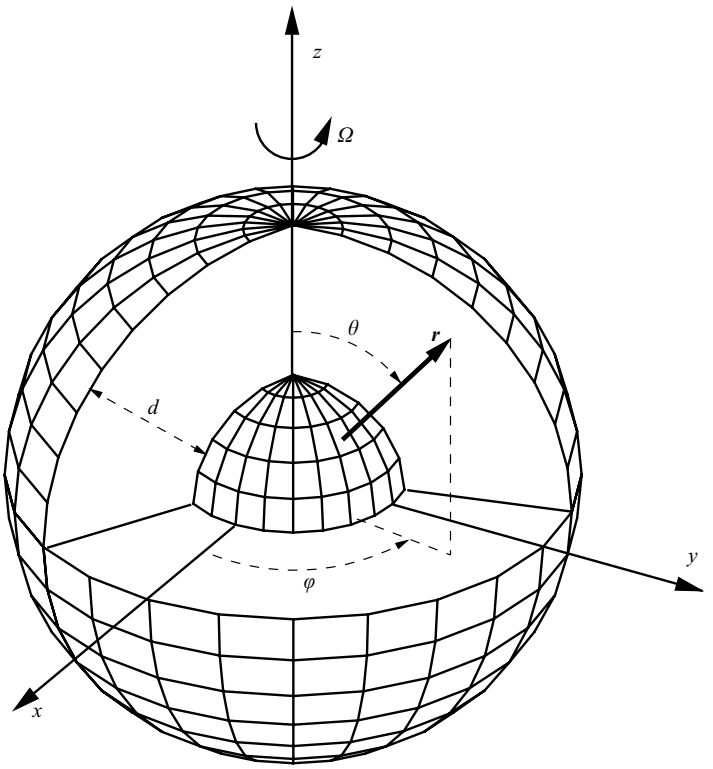


FIGURE 1. Geometrical configuration of the problem. A part of the outer spherical surface is removed to expose the interior of the shell to which the conducting fluid is confined.

diffusivities is simplistic there have not been many theoretical derivations for ratios of turbulent diffusivities which enter the dimensionless equations for the numerical simulations. Some theoretical considerations in the astrophysical context can be found in Eschrich & Rüdiger (1983). Values for an effective Prandtl number can eventually be derived from experiments on turbulent convection (see, for example, Ahlers & Xu 2001). Additional complications arise in planetary and astrophysical applications through anisotropies introduced by the effects of rotation and the presence of large-scale magnetic fields. While anisotropic eddy diffusivity tensors will be useful for more realistic models, for the purpose of the present paper we prefer the simplicity of scalar diffusivities.

After introducing the basic equations and the method of their numerical solution in § 2 we shall consider the most important properties of convection without magnetic field as a function of the Prandtl number in § 3. Since a number of earlier papers on this topic have been published, this section can be kept relatively short. In § 4, the onset of convection-driven dynamos in fluids with different Prandtl numbers is described. Energy aspects are considered in § 5 and the validity of the magnetostrophic approximation is discussed in § 6. The influences of various boundary conditions are considered in § 7 and a concluding discussion is given in § 8.

2. Mathematical formulation of the problem and methods of solution

We consider a rotating spherical fluid shell as shown in figure 1. We assume that a static state exists with the temperature distribution $T_S = T_0 - \beta d^2 r^2/2$. Here rd is

https://doi.org/10.1017/S0022112005004398 Published online by Cambridge University Press

the length of the position vector with respect to the centre of the sphere. The gravity field is given by $\boldsymbol{g} = -d\gamma\boldsymbol{r}$. In addition to d, the time d^2/ν, the temperature $\nu^2/\gamma\alpha d^4$ and the magnetic flux density $\nu(\mu\varrho)^{1/2}/d$ are used as scales for the dimensionless description of the problem where ν denotes the kinematic viscosity of the fluid, κ its thermal diffusivity, ϱ its density and μ is its magnetic permeability. The equations of motion for the velocity vector $\boldsymbol{u}$, the heat equation for the deviation Θ from the static temperature distribution, and the equation of induction for the magnetic flux density $\boldsymbol{B}$ are thus given by

$$\partial_t\boldsymbol{u} + \boldsymbol{u}\cdot\nabla\boldsymbol{u} + \tau\boldsymbol{k}\times\boldsymbol{u} = -\nabla\pi + \Theta\boldsymbol{r} + \nabla^2\boldsymbol{u} + \boldsymbol{B}\cdot\nabla\boldsymbol{B}, \tag{2.1a}$$

$$\nabla\cdot\boldsymbol{u} = 0, \tag{2.1b}$$

$$P(\partial_t\Theta + \boldsymbol{u}\cdot\nabla\Theta) = R\boldsymbol{r}\cdot\boldsymbol{u} + \nabla^2\Theta, \tag{2.1c}$$

$$\nabla\cdot\boldsymbol{B} = 0, \tag{2.1d}$$

$$\nabla^2\boldsymbol{B} = P_m(\partial_t\boldsymbol{B} + \boldsymbol{u}\cdot\nabla\boldsymbol{B} - \boldsymbol{B}\cdot\nabla\boldsymbol{u}), \tag{2.1e}$$

where ∂_t denotes the partial derivative with respect to time t and where all terms in the equation of motion that can be written as gradients have been combined into $\nabla\pi$. The Boussinesq approximation has been assumed in that the density ϱ is regarded as constant except in the gravity term where its temperature dependence given by $\alpha \equiv -(\mathrm{d}\varrho/\mathrm{d}T)/\varrho = \text{const.}$ is taken into account. The Rayleigh number R, the Coriolis number τ, the Prandtl number P and the magnetic Prandtl number P_m are defined by

$$R = \frac{\alpha\gamma\beta d^6}{\nu\kappa}, \quad \tau = \frac{2\Omega d^2}{\nu}, \quad P = \frac{\nu}{\kappa}, \quad P_m = \frac{\nu}{\lambda}, \tag{2.2}$$

where λ is the magnetic diffusivity. Because the velocity field $\boldsymbol{u}$ as well as the magnetic flux density $\boldsymbol{B}$ are solenoidal vector fields, the general representation in terms of poloidal and toroidal components can be used

$$\boldsymbol{u} = \nabla\times(\nabla v\times\boldsymbol{r}) + \nabla w\times\boldsymbol{r}, \tag{2.3a}$$

$$\boldsymbol{B} = \nabla\times(\nabla h\times\boldsymbol{r}) + \nabla g\times\boldsymbol{r}. \tag{2.3b}$$

By multiplying the (curl)^2 and the curl of (2.1a) by $\boldsymbol{r}$ we obtain two equations for v and w

$$[(\nabla^2 - \partial_t)\mathscr{L}_2 + \tau\partial_\varphi]\nabla^2 v + \tau\mathscr{Q}w - \mathscr{L}_2\Theta = -\boldsymbol{r}\cdot\nabla\times[\nabla\times(\boldsymbol{u}\cdot\nabla\boldsymbol{u} - \boldsymbol{B}\cdot\nabla\boldsymbol{B})], \tag{2.4a}$$

$$[(\nabla^2 - \partial_t)\mathscr{L}_2 + \tau\partial_\varphi]w - \tau\mathscr{Q}v = \boldsymbol{r}\cdot\nabla\times(\boldsymbol{u}\cdot\nabla\boldsymbol{u} - \boldsymbol{B}\cdot\nabla\boldsymbol{B}), \tag{2.4b}$$

where ∂_φ denotes the partial derivative with respect to the angle φ of a spherical system of coordinates r, θ, φ and where the operators $\mathscr{L}_2$ and $\mathscr{Q}$ are defined by

$$\mathscr{L}_2 \equiv -r^2\nabla^2 + \partial_r(r^2\partial_r),$$

$$\mathscr{Q} \equiv r\cos\theta\nabla^2 - (\mathscr{L}_2 + r\partial_r)(\cos\theta\partial_r - r^{-1}\sin\theta\partial_\theta).$$

The heat equation for the dimensionless deviation Θ from the static temperature distribution can be written in the form

$$\nabla^2\Theta + R\mathscr{L}_2 v = P(\partial_t + \boldsymbol{u}\cdot\nabla)\Theta, \tag{2.5}$$

and the equations for h and g are obtained through the multiplication of (2.1e) and of its curl by $\boldsymbol{r}$

$$\nabla^2\mathscr{L}_2 h = P_m[\partial_t\mathscr{L}_2 h - \boldsymbol{r}\cdot\nabla\times(\boldsymbol{u}\times\boldsymbol{B})], \tag{2.6a}$$

$$\nabla^2\mathscr{L}_2 g = P_m[\partial_t\mathscr{L}_2 g - \boldsymbol{r}\cdot\nabla\times(\nabla\times(\boldsymbol{u}\times\boldsymbol{B}))]. \tag{2.6b}$$

https://doi.org/10.1017/S0022112005004398 Published online by Cambridge University Press

We assume stress-free boundaries with fixed temperatures and use the value 0.4 for the radius ratio $\eta = r_i/r_o$,

$$v = \partial_{rr}^2 v = \partial_r(w/r) = \Theta = 0 \qquad \text{at } r = r_i \equiv 2/3, \quad r = r_o \equiv 5/3. \tag{2.7}$$

For the magnetic field, electrically insulating boundaries are assumed such that the poloidal function h must be matched to the function $h^{(e)}$ which describes the potential fields outside the fluid shell

$$g = h - h^{(e)} = \partial_r\left(h - h^{(e)}\right) = 0 \quad \text{at } r = r_i \equiv 2/3, \quad r = r_o \equiv 5/3. \tag{2.8}$$

But computations for the case of an inner boundary with no-slip conditions and an electrical conductivity equal to that of the fluid have also been done. The numerical integration of equations (2.4), (2.5) and (2.6) together with boundary conditions (2.7) and (2.8) proceeds with the pseudospectral method as described by Tilgner & Busse (1997) which is based on an expansion of all dependent variables in spherical harmonics for the θ, φ dependences, i.e.

$$v = \sum_{l,m} V_l^m(r,t) P_l^m(\cos\theta) \exp\{\mathrm{i}m\varphi\} \tag{2.9}$$

and analogous expressions for the other variables, w, Θ, h and g. P_l^m denotes the associated Legendre functions. For the r-dependence, expansions in Chebychev polynomials are used. For further details see also Busse, Grote & Tilgner (1998) or Grote, Busse & Tilgner (1999). For the computations to be reported in the following, a minimum of 33 collocation points in the radial direction and spherical harmonics up to the order 64 have been used; but in many cases, the resolution has been increased to 49 collocation points and spherical harmonics up to the order 96 or 128.

3. Convection in rotating spherical shells

Three different types of convection can be distinguished in rotating spherical shells. Predominantly convection occurs in the form of rolls aligned with the axis of rotation which exhibit properties of thermal Rossby waves in that they are drifting in the prograde azimuthal direction. They are confined to the region outside the virtual surface of the tangent cylinder which touches the inner boundary at its equator. The dynamics of these convection columns, as they are sometimes called, is intimately connected for Prandtl numbers of the order unity or less with the differential rotation that is generated by their Reynolds stresses. Above their onset as an m-periodic pattern in the azimuthal direction, the convection columns experience, with increasing Rayleigh number, transitions to amplitude and shape vacillations before they become spatio-temporally chaotic in the dimensions perpendicular to the axis while retaining their nearly perfect alignment with the rotation vector. In this regime of beginning turbulence, coherent processes such as localized convection and relaxation oscillations are realized through the interaction of the differential rotation and the convection columns. A graphical display of these stages of convection is shown in figure 2 in terms of the streamlines of the convection columns intersected by the equatorial plane. For a more detailed description we refer to Grote & Busse (2001) or the review of Busse (2002*a*). As the Reynolds stresses decrease with increasing P these coherent processes disappear. Figure 3 indicates that the spiralling nature of the convection columns also diminishes with increasing Rayleigh number. A small non-geostrophic

https://doi.org/10.1017/S0022112005004398 Published online by Cambridge University Press

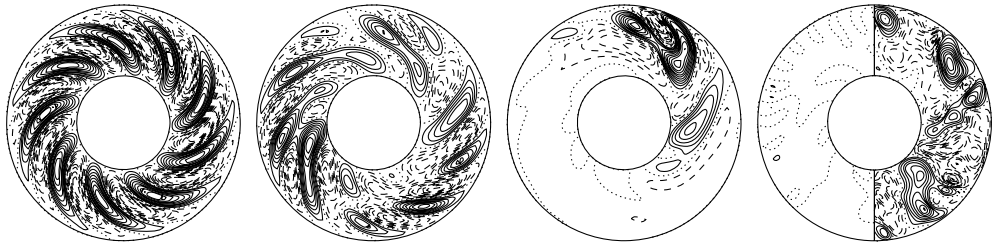


FIGURE 2. Equatorial streamlines $r\partial_\varphi v = \text{const.}$ in the case $P = 0.5$, $\tau = 10^4$ and $R = 1.8 \times 10^5$ 3.2×10^5, 4×10^5, 9×10^5 (from left to right). The two halves of the last plot show convection in the minimum and in the maximum of a relaxation cycle.



FIGURE 3. Equatorial streamlines $r\partial_\varphi v = \text{const.}$ in the case $P = 20$, $\tau = 5 \times 10^3$ and $R = 1.6 \times 10^5$, 1.75×10^5, 2.5×10^5, 1.5×10^6 (from left to right).

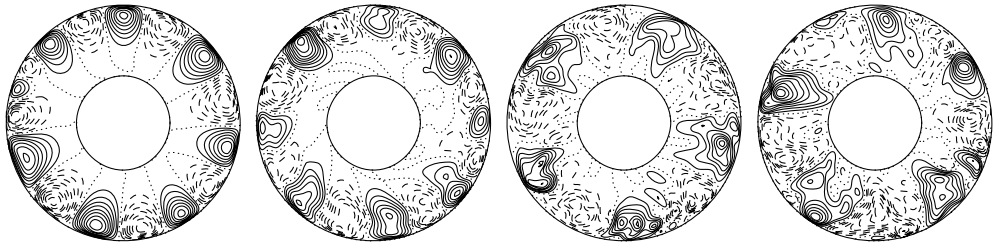


FIGURE 4. Equatorial streamlines $r\partial_\varphi v = \text{const.}$ in the case $P = 0.025$, $\tau = 10^5$ and $R = 4 \times 10^5$, 6×10^5, 8×10^5, 10^6 (from left to right).

differential rotation persists driven as a 'thermal wind' by temperature gradients caused by the lateral inhomogeneity of the convective heat transport.

A second distinct form of convection is the equatorially attached cells which represent modified inertial modes and become the preferred form of convection at sufficiently low values of P. They were first found by Zhang & Busse (1987) and analytical descriptions in terms of perturbed inertial oscillations have been given by Zhang (1994, 1995) and Busse & Simitev (2004). The equatorially attached cells do not develop strong Reynolds stresses and they are thus less subject to the disruptive effects of the shear of a differential rotation. However, the continuity of the convective heat transport requires that the equatorially attached convection occurs in conjunction with the columnar convection closer to the inner boundary of the shell. This effect is visible in the form of secondary extrema of the streamlines far from the boundary in figure 4 where the evolution of the convection flows in the chaotic regime is illustrated. Note that the strong attachment to the outer equatorial boundary persists even at the highest value of R used in this figure. For further details see Simitev & Busse (2003).

https://doi.org/10.1017/S0022112005004398 Published online by Cambridge University Press

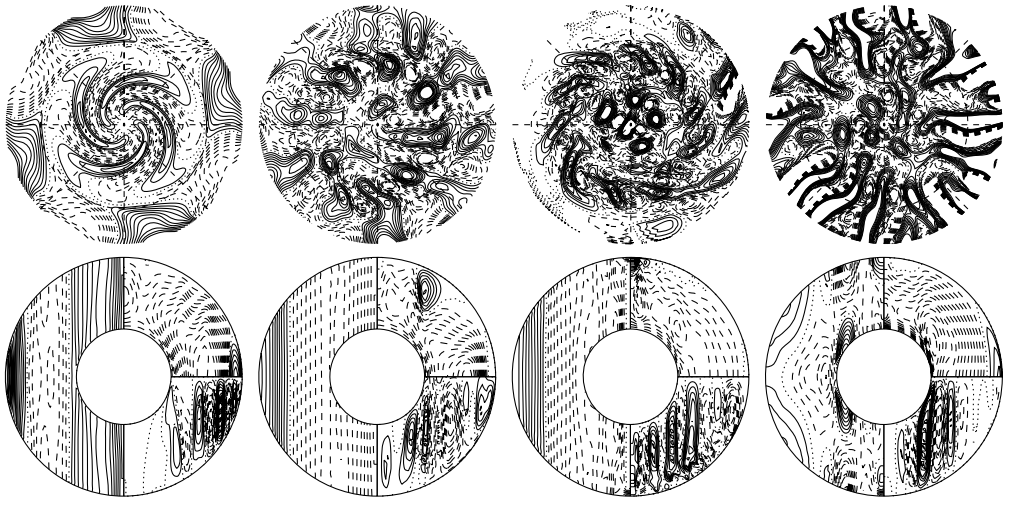


FIGURE 5. Polar convection in the cases $P=0.025$, $\tau=5\times10^4$, $R=2\times10^5$; $P=0.1$, $\tau=3\times10^4$, $R=7.5\times10^5$; $P=1$, $\tau=10^4$, $R=1.4\times10^6$ and $P=20$, $\tau=5\times10^3$, $R=10^6$ (from left to right). The plots in the upper row show lines of constant u_r at the surface $r=r_i+0.5$ as seen from the north pole. Isolines corresponding to higher amplitude have not been plotted in order to emphasize structures with lower amplitude. The plots in the lower row exhibit lines of constant $\overline{u}_\varphi$ in the left half, of $\overline{\Theta}$ in the upper right quarter and of the streamlines $r\sin\theta\partial_\theta\overline{v}$ in the lower right quarter, all in the meridional plane.

A third form of convection is realized in the polar regions of the shell which comprise the two fluid domains inside the tangent cylinder. Since gravity and rotation vectors are nearly parallel in these regions (unless large values of η are used) convection resembles the kind realized in a horizontal layer heated from below and rotating about a vertical axis. A tendency towards an alignment of convection rolls with the North–South direction (Busse & Cuong 1977) can be noticed, but this property is superseded by instabilities of the Küppers–Lortz type and by interactions with turbulent convection outside the tangent cylinder. The onset of convection in the polar regions generally occurs at Rayleigh numbers considerably above the critical values R_c for onset of convection outside the tangent cylinder. Except for the case of very low Prandtl numbers, the differential rotation in the polar regions is usually oriented in the direction opposite to that of rotation and thus tends to facilitate polar convection by reducing the rotational constraint. The possibility exists, however, that at sufficiently low values of P and high values of τ, finite-amplitude convection in the polar regions may precede the onset of convection in other regions. The patterns of polar convection and other properties discussed in this section are illuminated by the display of convection at different values of P in figure 5.

Quantitative aspects of convection are described by figure 6 where the averages over space and time of the kinetic energy densities of the various components of the convection flow are shown as a function of R. The energy densities are defined by

$$\overline{E}_p=\tfrac{1}{2}\langle|\,\nabla\times(\nabla\bar{v}\times\boldsymbol{r})\,|^2\rangle,\quad \overline{E}_t=\tfrac{1}{2}\langle|\,\nabla\bar{w}\times\boldsymbol{r}\,|^2\rangle, \tag{3.1a}$$

$$\check{E}_p=\tfrac{1}{2}\langle|\,\nabla\times(\nabla\check{v}\times\boldsymbol{r})\,|^2\rangle,\quad \check{E}_t=\tfrac{1}{2}\langle|\,\nabla\check{w}\times\boldsymbol{r}\,|^2\rangle, \tag{3.1b}$$

where the angle brackets indicate the average over the fluid shell and $\bar{v}$ refers to the azimuthally averaged component of v, while $\check{v}$ is defined by $\check{v}=v-\bar{v}$. The Nusselt

https://doi.org/10.1017/S0022112005004398 Published online by Cambridge University Press

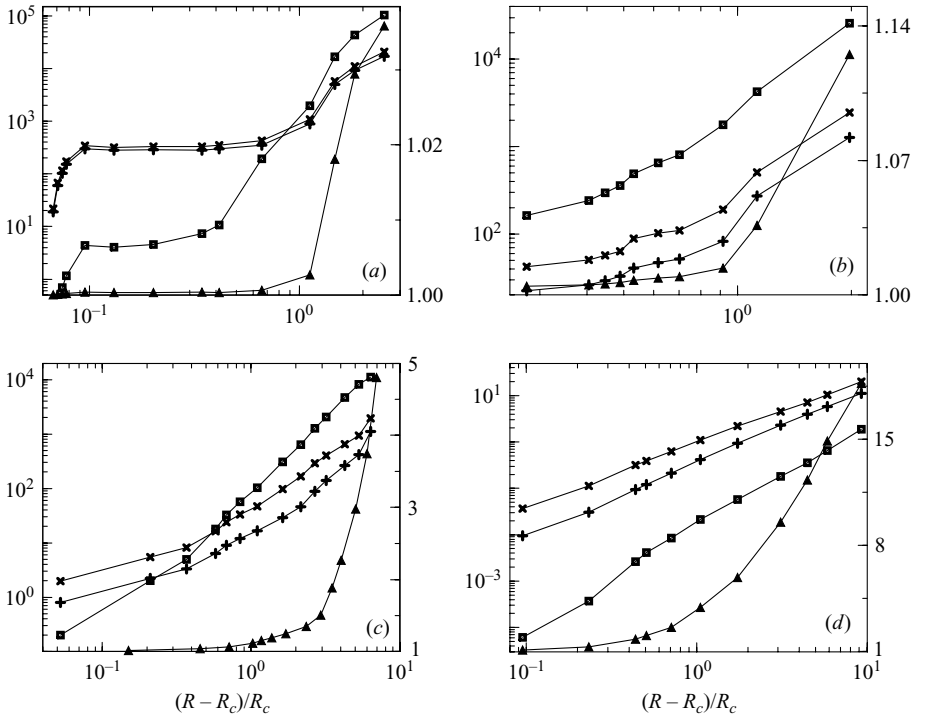


FIGURE 6. Time-averaged energy densities $\overline{E}_t$ (squares), $\check{E}_p$ (plus-signs), $\check{E}_t$ (crosses) and Nusselt number Nu_i (filled triangles, right ordinates) as functions of $(R-R_c)/R_c$ for (*a*) $P=0.025$, $\tau=10^5$, (*b*) $P=0.1$, $\tau=3\times10^4$, (*c*) $P=1$, $\tau=10^4$, and (*d*) $P=20$, $\tau=5\times10^3$. The values of R_c are 283 000, 235 000, 190 000 and 146 000 in the cases (*a*), (*b*), (*c*) and (*d*), respectively. The mean poloidal energy component $\overline{E}_p$ has been omitted since it is by factor 10^3–10^2 smaller than the other components.

number at the inner spherical boundary Nu_i is also shown in figure 6. It is defined by

$$Nu_i = 1 - \frac{P}{r_i}\left.\frac{\mathrm{d}\overline{\overline{\Theta}}}{\mathrm{d}r}\right|_{r=r_i}, \tag{3.2}$$

where the double bar indicates the average over the spherical surface. The rapid growth with R of $\overline{E}_t$ corresponding to the energy of differential rotation is remarkable in the cases (*a*), (*b*) and (*c*) of figure 6. Only for higher values of P as in case (*d*) does $\overline{E}_t$ never exceed the energies of the fluctuating components of motion. Another remarkable feature of the plots is the rapid rise of the Nusselt number Nu_i after the onset of amplitude vacillations and the transition to a chaotic time dependence. The steadily drifting convection columns or the equatorially–attached cells do not transport heat very well because of the mismatch between the geometry of the boundaries and the flow structure. Because this mismatch does not occur in the case of polar convection, the heat transport of the latter may easily exceed that of convection outside the tangent cylinder at higher values of R. The dependence of the kinetic energy densities on R in case (*a*) of figure 6 are somewhat unusual in that, after a rapid growth near onset, a regime of saturation follows and a growth of the kinetic energies with R begins again only when R has reached nearly twice its critical value. The behaviour is caused by the competition of several modes with different

https://doi.org/10.1017/S0022112005004398 Published online by Cambridge University Press

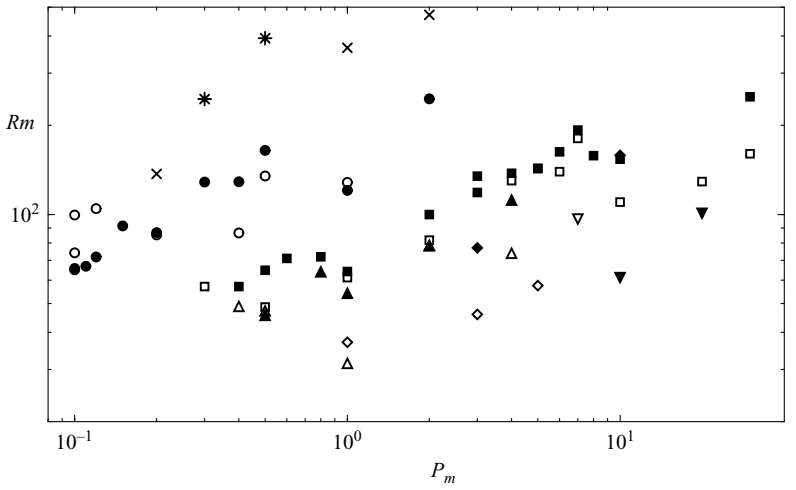


FIGURE 7. Magnetic Reynolds numbers Rm for the onset of dynamo action as a function of P_m in the cases $P=0.01$, $\tau=10^5$ (stars), $P=0.025$, $\tau=10^5$ (crosses), $P=0.1$, $\tau=10^5$ (circles), $P=1$, $\tau=3\times10^4$ (triangles up), $P=1$, $\tau=10^4$ (squares) and $P=5$, $\tau=5\times10^3$ (diamonds) and $P=10$, $\tau=5\times10^3$ (triangles down). The open symbols in the cases with $P\geqslant0.1$ are based on decaying dynamos, the filled symbols are based on the lowest non-decaying solutions.

azimuthal wavenumbers m as is described in more detail by Simitev & Busse (2003). The ways in which properties of convection are reflected in the generated magnetic fields will be discussed in the following sections.

4. The onset of dynamo action for different Prandtl numbers

The onset of convection-driven dynamos in the case $P=1$ has been explored in numerous papers in the past. We refer to the work of Kageyama & Sato (1997), Busse, Grote & Tilgner (1998), Kida & Kitauchi (1998), Christensen, Olson & Glatzmaier (1999), Olson, Christensen & Glatzmaier (1999), Katayama, Matsushima & Honkura (1999), Grote, Busse & Tilgner (2000), Grote & Busse (2001), Ishihara & Kida (2002), Busse, Grote & Simitev (2003) and Takahashi, Matsushima & Honkura (2003). In particular, the results of Grote *et al.* and Grote & Busse can be compared well with the results presented in the following since only the Prandtl number differs among the parameters of the computations. Since one of the goals of the numerical simulations is the search for dynamos with low values of the magnetic Prandtl number P_m, the amplitude of convection must be sufficiently high that the magnetic Reynolds number defined by $Rm=(2E)^{1/2}P_m$ reaches a value of the order 10^2. Here E refers to the average density of the kinetic energy of convection, i.e. $E=\overline{E}_p+\overline{E}_t+\breve{E}_p+\breve{E}_t$. In figure 7, values of Rm for cases of sustained dynamo action and for cases of decaying magnetic fields have been indicated for several values of P. No special effort has been made to determine the minimum value Rm_{min} of Rm for dynamo action. Since in all cases convection is chaotic and since dynamos are typically subcritical, i.e. the boundary between sustenance of a dynamo and its decay occurs at finite amplitudes of the magnetic field, Rm_{min} is not a well-defined quantity. Moreover, the value Rm as defined above will decrease after the onset of dynamo action since typically the energy of differential rotation is strongly reduced by the action of the Lorentz force.

It is evident from figure 7 that the goal of low values of P_m is most readily reached at low Prandtl numbers. At high values of P, the minimum value of the magnetic

https://doi.org/10.1017/S0022112005004398 Published online by Cambridge University Press

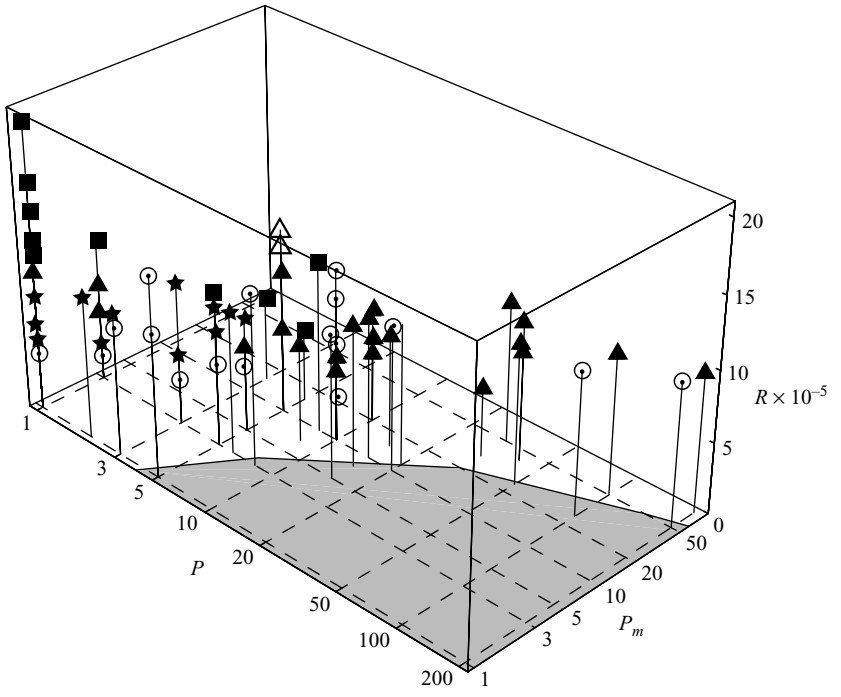


FIGURE 8. Convection-driven dynamos as a function of R, P and P_m for $\tau = 5 \times 10^3$. The symbols indicate chaotic dipolar (▲), hemispherical (△), quadrupolar (★), mixed (■) and decaying dynamos (⊙).

Reynolds numbers for dynamos decreases slightly, but P_m must increase in proportion to P in order to achieve a finite ratio P/P_m in the limit of infinite Prandtl number, as shown by Zhang and Busse (1990). The tendency of low Prandtl numbers to lower the minimum values of P_m required for dynamos is limited, however, by the transition to inertial convection for $P \leqslant (\tau/\tau_0)^{-2}$ where τ_0 is a quantity of the order 10^2 (Ardes, Busse & Wicht 1997). It thus has not been possible to obtain dynamos with values of P_m below 0.1 for Prandtl numbers less than 0.05. Inertial convection is evidently less conducive to dynamo action than columnar convection and higher values of R_m are required for dynamos at $P = 0.025$ and $P = 0.01$ than at higher Prandtl numbers, according to figure 7. The most promising way towards low P_m dynamos thus appears to be an increasing τ with an accompanying reduction of P. Of course, the numerical resolution will have to be increased at the same time.

A particular feature that is evident from figure 7 (and also figure 9) is that high values of R may prevent dynamo action. In the case $P = 0.1$, $\tau = 10^5$, it is found that only a finite interval of convection energy permits dynamo action since high values of Rm lead to the expulsion of magnetic flux from the convection eddies which is detrimental for the generation of magnetic fields. The same effect can also be seen for higher values of the Prandtl number as demonstrated in the case of $P_m = P = 10$ of figure 8.

A more complete overview of dynamos at values of P and P_m above unity is shown in figure 8 where the structure of the magnetic field is also indicated. As long as the properties of convection are nearly symmetric with respect to the equatorial plane three types of dynamo can be distinguished. Quadrupolar dynamos are characterized

https://doi.org/10.1017/S0022112005004398 Published online by Cambridge University Press

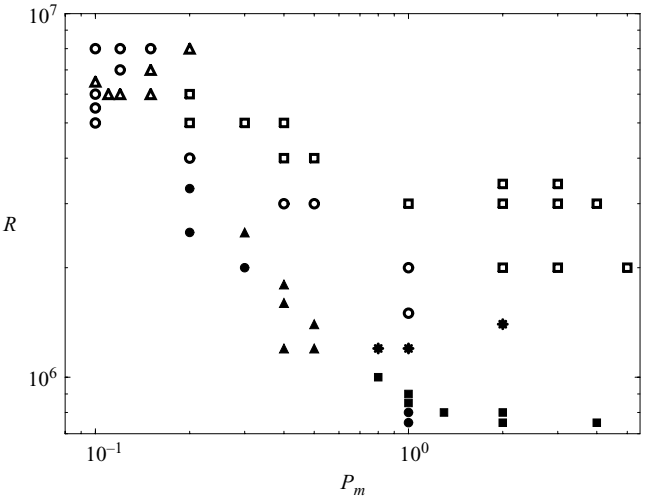


FIGURE 9. Convection-driven dynamos as a function of the Rayleigh number R and the magnetic Prandtl number P_m for $P = 0.1$, $\tau = 10^5$ (open symbols) and $\tau = 3 \times 10^4$ (filled symbols). The symbols indicate chaotic dipolar (squares), hemispherical (triangles), mixed (stars) and decaying dynamos (circles).

by a magnetic field that exhibits the same symmetry with respect to the equatorial plane as the convection velocity field, while the opposite symmetry characterizes dipolar dynamos. Hemispherical dynamos correspond to the superposition of a quadrupolar and a dipolar magnetic field of nearly the same form, but with opposite signs in the northern and the southern hemispheres such that the magnetic field nearly vanishes in one of the hemispheres (Grote & Busse 2000). Once the symmetry of convection with respect to the equatorial plane is impaired significantly – as happens, for example, at higher Rayleigh numbers through the onset of polar convection – the structures of dynamos can no longer be clearly distinguished and we speak of 'mixed' dynamos. These dynamos continue to exhibit an alignment with the axis of rotation. Dynamos with a dominant equatorial dipole, for instance, have not been found.

For a fixed value of P, quadrupolar dynamos are obtained for sufficiently low values of P_m which give way to hemispherical and dipolar dynamos with increasing P_m as has also been observed in the case $P = 1$ (Grote, Busse & Tilgner 2000). However, since dynamos for low values of P_m disappear with increasing P, quadrupolar and hemispherical dynamos can no longer be obtained as P exceeds a value of the order 5 in the case of $\tau = 5 \times 10^3$. Quadrupolar dynamos thus appear to be restricted to Prandtl numbers of order unity and moderate values of τ. When τ is increased from 10^4 to 3×10^4, quadrupolar dynamos no longer seem to be accessible according to the results of Grote, Busse & Simitev (2001, see also Busse 2002*a*). The same effect occurs as P is lowered, as indicated in figure 9 for the case $P = 0.1$, $\tau = 10^5$. Here the lowest value of P_m corresponds to a hemispherical dynamo.

It should be noted that the critical value R_c of the Rayleigh number increases nearly in proportion to τP for $P < 1$ and nominally higher values of τ can thus be reached for lower values of P. The degree of chaos increases, however, with decreasing P because of the short thermal time scale. Nevertheless, coherent structures are also found such as the relaxation oscillations apparent in the time record shown in figure 10. Here the energy densities on the various components of the magnetic field are shown which

https://doi.org/10.1017/S0022112005004398 Published online by Cambridge University Press

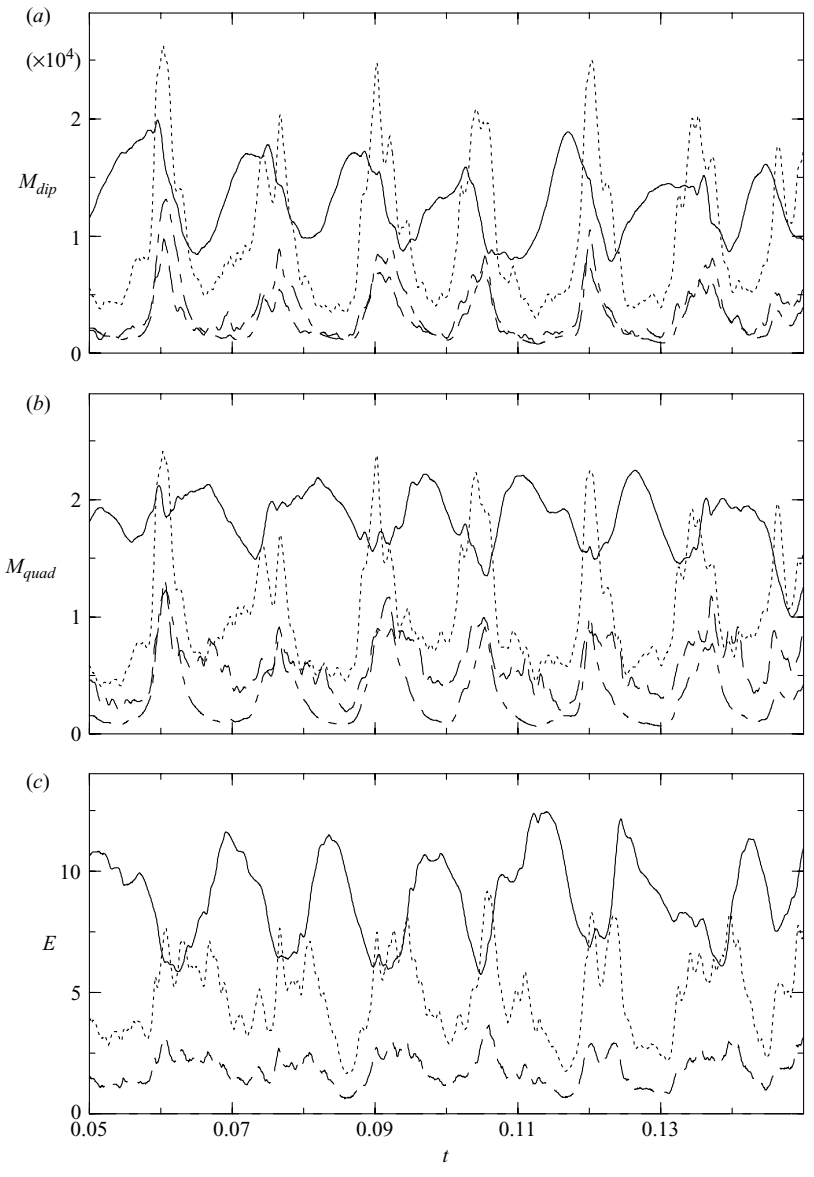


FIGURE 10. Time series of energy densities of a hemispherical dynamo in the case $P = 0.1$, $\tau = 10^5$, $R = 6 \times 10^6$, $P_m = 0.11$. (a, b) Energy densities of dipolar and quadrupolar components of the magnetic field, (c) energy densities of the velocity field. The mean toroidal components are represented by solid lines, the fluctuating toroidal by dotted lines, the mean poloidal by dot-dashed lines and the fluctuating poloidal by dashed lines.

are defined in analogy to the kinetic energy densities (3.1),

$$\overline{M}_p = \tfrac{1}{2}\langle |\, \nabla \times (\nabla \bar{h} \times \boldsymbol{r})\, |^2 \rangle, \quad \overline{M}_t = \tfrac{1}{2}\langle |\, \nabla \bar{g} \times \boldsymbol{r}\, |^2 \rangle, \tag{4.1a}$$

$$\check{M}_p = \tfrac{1}{2}\langle |\, \nabla \times (\nabla \check{h} \times \boldsymbol{r})\, |^2 \rangle, \quad \check{M}_t = \tfrac{1}{2}\langle |\, \nabla \check{g} \times \boldsymbol{r}\, |^2 \rangle. \tag{4.1b}$$

In contrast to the relaxation oscillations of non-magnetic convection mentioned in connection with figure 2 the oscillations of figure 10 have a much shorter period

https://doi.org/10.1017/S0022112005004398 Published online by Cambridge University Press

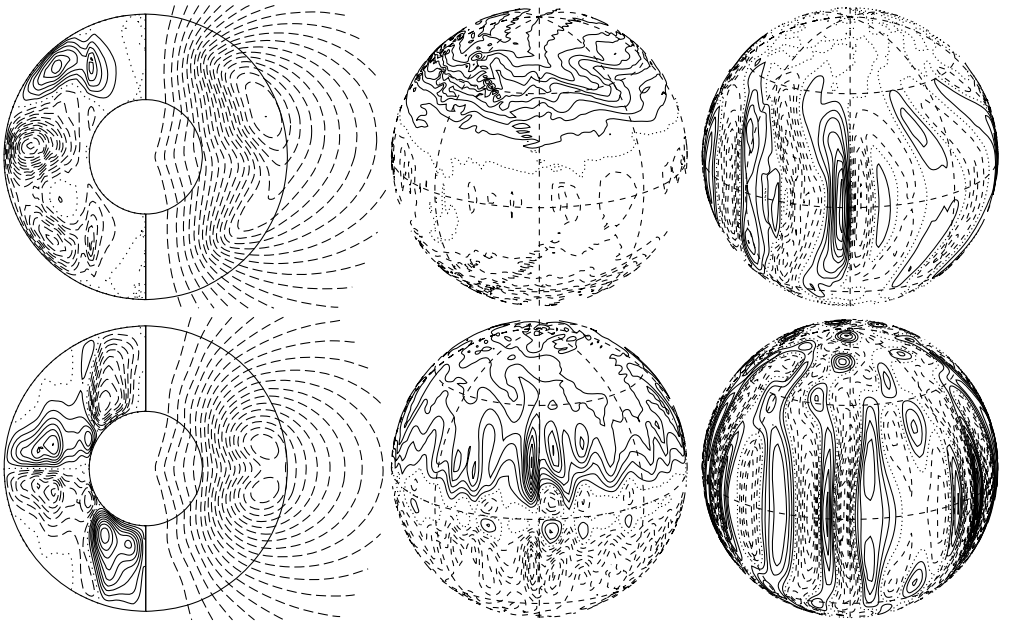


FIGURE 11. Non-oscillatory chaotic dipolar dynamos in the cases $P=0.1$, $\tau=10^5$, $R=2\times10^6$, $P_m=3$ (upper row) and $P=200$, $\tau=5\times10^3$, $R=10^6$, $P_m=80$ (lower row). The left-hand column shows meridional isolines of $\overline{B}_\varphi$ (left half) and of $r\sin\theta\partial_\theta\overline{h}$ (right half). The middle column shows lines $B_r=$ const. at $r=r_0$. The right-hand column shows lines $u_r=$ const. at $r=r_i+0.5$.

and originate from the oscillations of the hemispherical magnetic field, as is evident from the comparable periods. Since the strength of the magnetic field varies more with the phase of the cycle at low values of P than at higher ones, the action of the Lorentz force on the differential rotation also exhibits significant variations. This, in turn, affects the amplitude of convection and its dynamo action and leads to the cyclic feedback process evident in figure 10. We note that the computational results displayed in figure 10 were obtained with a resolution of 33 collocation points in the radial direction and with spherical harmonics of the order 96. Results obtained with 41 collocation points and spherical harmonics up to the order 108 are rather similar and the time-averaged energies differ insignificantly.

Finally, we would like to point out some typical differences between high- and low-Prandtl-number dipolar dynamos which are exhibited by the plots of figure 11. At low values of P, the quadrupolar component is usually quite noticeable, leading to a shift of the magnetic equator away from the geometric one. Often this shift alternates in time in a nearly periodic fashion. In high-Prandtl-number dynamos, the mean magnetic field is nearly steady and the quadrupolar component is negligible if the Rayleigh number is not too high. This is evident in the lower plots of figure 11 even though the onset of polar convection with its attendant asymmetry with respect to the equatorial plane can already be seen. A characteristic feature of high P dynamos are the strong zonal magnetic flux tubes in the polar regions which are mainly caused by the thermal wind shear, an example of which can be seen in the case $P=20$ of figure 5. These flux tubes are also very evident in the dynamo of Glatzmaier & Roberts (1995). While the differential rotation changes a lot with increasing Prandtl number, the structure of the convection columns hardly varies, as is also evident

https://doi.org/10.1017/S0022112005004398 Published online by Cambridge University Press

from figure 11. The rate of drift in the azimuthal direction decreases, of course, with increasing P.

5. Energetics of dynamos

It is of interest to compare the various interactions between velocity and magnetic field components which sustain dynamo action against ohmic dissipation. Zhang & Busse (1989) have listed a total of 31 interaction integrals which contribute to the energy balances obtained from (2.6) for the mean and fluctuating components of the poloidal and toroidal magnetic fields. Fortunately, only a few of the 31 terms contribute significantly and we list here only the most important ones,

$$\bar{p}_1 \equiv (\check{v}\check{g}\bar{h}), \qquad \bar{p}_2 \equiv (\check{w}\check{h}\bar{h}), \qquad \bar{p}_3 \equiv (\check{v}\check{h}\bar{h}), \tag{5.1a}$$

$$\bar{t}_1 \equiv (\bar{w}\bar{h}\bar{g}), \qquad \bar{t}_2 \equiv (\check{w}\check{h}\bar{g}), \qquad \bar{t}_3 \equiv (\check{v}\check{g}\bar{g}), \tag{5.1b}$$

$$\check{p}_1 \equiv (\check{v}\bar{g}\check{h}), \qquad \check{p}_2 \equiv (\check{v}\check{g}\check{h}), \qquad \check{p}_3 \equiv (\check{v}\check{h}\check{h}), \tag{5.1c}$$

$$\check{t}_1 \equiv (\check{w}\bar{g}\check{g}), \qquad \check{t}_2 \equiv (\check{w}\check{g}\check{g}), \qquad \check{t}_3 \equiv (\check{w}\bar{h}\check{g}), \tag{5.1d}$$

where the first two letters inside the parentheses indicate which of the interactions between velocity and magnetic field components on the right-hand sides of (2.6) counteract the ohmic dissipation of the magnetic field component indicated by the last letter inside the brackets. In the case of chaotic dynamos these integrals tend to fluctuate wildly and may change their signs. The particular ones listed above have been plotted as a function of time in figure 12 together with the corresponding average ohmic dissipation density for three representative cases. It is remarkable that the differential rotation contributes most of the sustenance of the mean toroidal field not only in the case of low values of P and P_m, but also in the high-Prandtl-number case. The mean thermal wind is obviously sufficient to generate the mean toroidal field through the distortion and stretching of the mean poloidal field. This ω-effect is thus usually found to dominate the dynamo process in the case of the zonal field. Only in particularly chaotic dynamos characterized by a rather weak mean poloidal field is the ω-effect not effective, as in the case $P = 0.1$, $P_m = 3$ of figure 12. It is remarkable that the first and second terms of definitions (5.1a) are strongly anticorrelated in the low-Prandtl-number cases of figure 12. Because of their near cancellations, the axisymmetric poloidal field is rather weak in low P dynamos.

The α-effect in which the fluctuating magnetic field is generated through the interaction between fluctuating velocity field and mean magnetic field plays a far less important role than the ω-effect. The fluctuating components of the magnetic field are usually generated through interactions of fluctuating parts of velocity and magnetic fields except in the case of high Prandtl numbers where the mean poloidal field typically dominates.

One of the least understood questions of convection-driven dynamos is the equilibration of magnetic energy. While in the astrophysical context an equipartition between kinetic and magnetic energy is often favoured, an Elsasser number Λ of order unity is regarded by geophysicists as a good estimate of the magnetic energy generated by dynamos in planetary cores. In the following, we shall use the definition

$$\Lambda = \frac{2M P_m}{\tau} \tag{5.2}$$

for the Elsasser number, where M denotes the magnetic energy density averaged over the fluid shell and in time, i.e. $M = \overline{M}_p + \overline{M}_t + \check{M}_p + \check{M}_t$. Chandrasekhar (1961)

https://doi.org/10.1017/S0022112005004398 Published online by Cambridge University Press

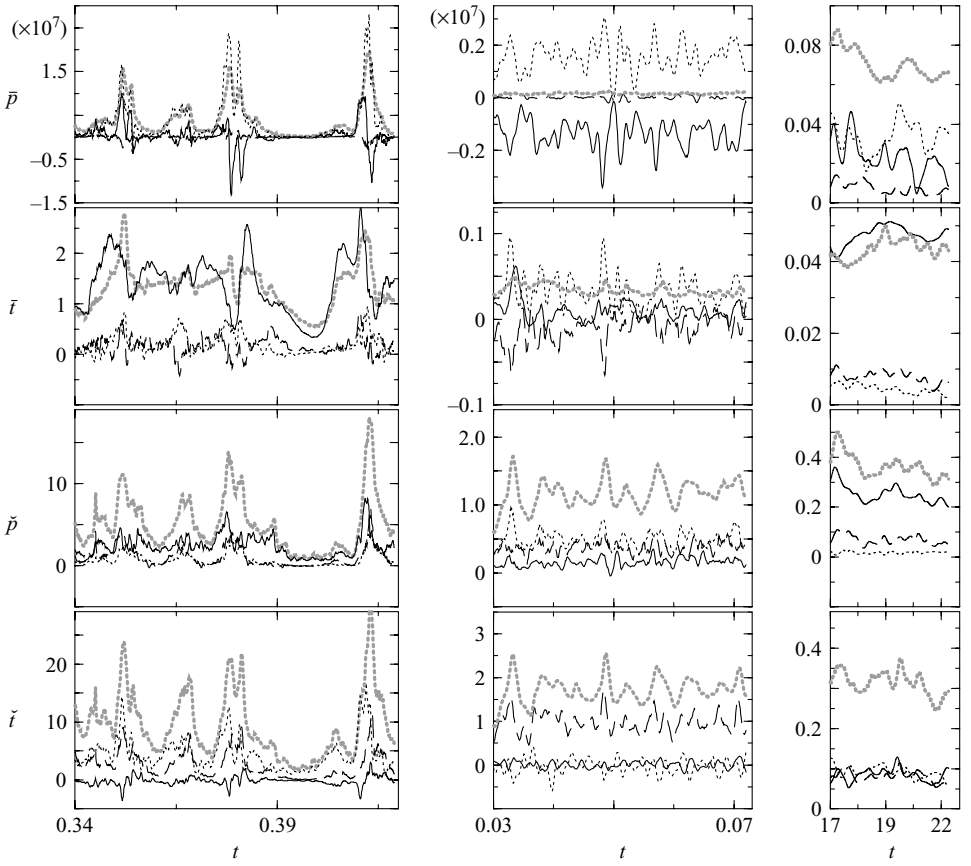


FIGURE 12. Lorentz terms (the thin solid, dotted and dashed lines indicate the first, second and third terms, respectively, in each of the lines of (5.1)) and Ohmic dissipations (thick dotted shaded lines) in the cases $P = 0.1$, $\tau = 10^5$, $R = 6 \times 10^6$, $P_m = 0.15$ (left-hand column), $P = 0.1$, $\tau = 10^5$, $R = 3 \times 10^6$, $P_m = 3$ (middle column), $P = 200$, $\tau = 5 \times 10^3$, $R = 10^6$, $P_m = 80$ (right-hand column).

established that, for $\Lambda = 1$, a minimum is found of the critical Rayleigh number for onset of convection in a horizontal layer heated from below, penetrated by a homogeneous vertical magnetic field and rotating about a vertical axis.

In figures 13 and 14, averaged kinetic and magnetic energy densities and viscous and ohmic dissipation densities have been plotted for typical parameter sets of the problem. The Elsasser number has been computed for the largest magnetic energy M in each of the boxes and is given in the figure captions. It is evident that Λ rarely exceeds unity and when it does, a physical reason of a high value of Λ is not obvious. In particular, in the cases of figure 13 where only P_m is varied, it is hard to understand why the Elsasser number increases more strongly than P_m itself. Another way of looking at the problem is to determine the highest value of Λ as a function of the Rayleigh number. A systematic study of the variation of magnetic energies with increasing R has been undertaken by Grote & Busse (2001) in the case $P = P_m = 1$, $\tau = 5 \times 10^3$. This study has been extended since that time in order to obtain reliable time averages, see figure 11 of Busse & Simitev (2005). Here the case of maximal M is attained for $R = 1.4 \times 10^6$ in figure 14(*e*) and corresponds to a value of about unity

https://doi.org/10.1017/S0022112005004398 Published online by Cambridge University Press

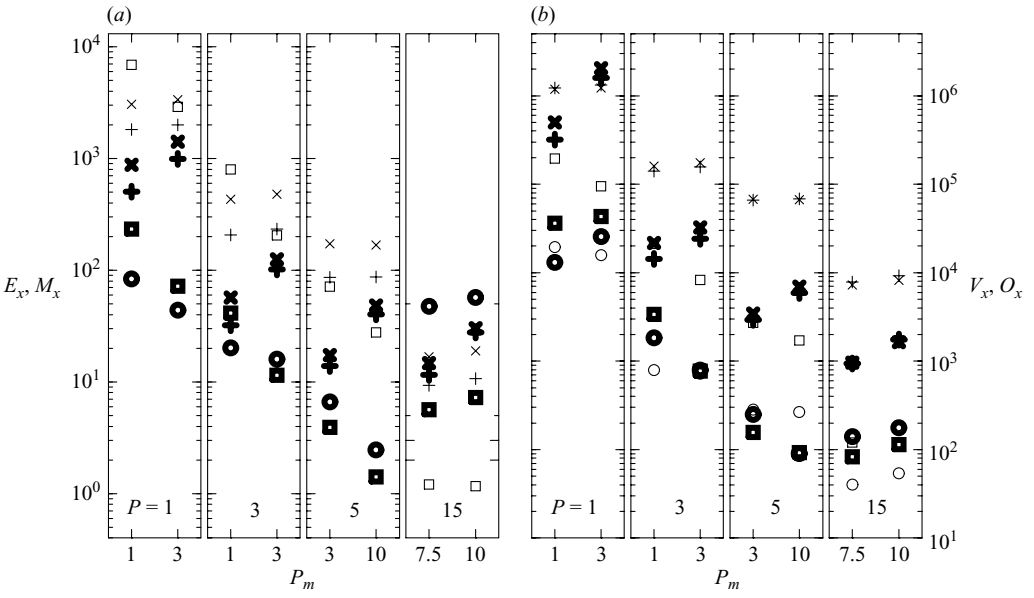


FIGURE 13. (*a*) Kinetic E_x and magnetic M_x energy densities and (*b*) viscous V_x and ohmic O_x dissipations as functions of P_m for convection-driven dynamos for $\tau = 5 \times 10^3$, $R = 10^6$ and Prandtl number as indicated in the boxes. The highest values of the Elsasser number for the cases $P = 1$, 3, 5 and 15 are $\Lambda = 3.02$, 0.31, 0.37 and 0.49, respectively. The components $\overline{X}_p$, $\overline{X}_t$, $\check{X}_p$, $\check{X}_t$ (where $X = E$, M, V, O) are represented by circles, squares, plus-signs and crosses, respectively. Kinetic energy densities and viscous dissipations are shown with light symbols, magnetic energy densities and ohmic dissipations are shown with heavy symbols.

for Λ; but this result may be accidental as is suggested by the magnetic fields in the cases of dynamos for low values of P and P_m. Here again we find in figure 14(*a*) that magnetic energy has reached a value close to its maximum as a function of R, but the corresponding value 0.38 of Λ is significantly lower. A much higher value of Λ is obtained, on the other hand, when $P_m = 0.2$ is replaced by $P_m = 3$, even though M may still increase with a further increase in R. We thus conclude that the criterion $\Lambda \approx 1$ for the equilibration of the magnetic energy is useful as a rough estimate, but the dependence of the equilibrium magnetic energy on P_m is actually weaker than suggested by the definition (5.2) of Λ.

There are a number of other features exhibited by figures 13 and 14. While the energy densities of the fluctuating components of the magnetic field usually exceed those of the mean components, this situation is reversed at sufficiently high Prandtl numbers for the poloidal part of the field, as is evident from the last columns of figure 13 as well as of figure 14. This changeover occurs suddenly at about $P = 8$ for $\tau = 5 \times 10^3$ as can be seen in the comparison of cases (*f*) and (*g*) of figure 14. A closer inspection shows that the replacement of the geostrophic differential rotation by the thermal wind and the accompanying growth of the polar zonal flux tubes is responsible for this change in the dynamo process. It should be noted that this changeover is not evident in the plots of the dissipation densities since the latter are always much lower for the mean components than for the fluctuating components.

Another property that changes with increasing Prandtl number is that for P of order unity or less, the energy of the mean toroidal field exceeds that of the mean poloidal field except for some high-Rayleigh-number cases where polar convection

https://doi.org/10.1017/S0022112005004398 Published online by Cambridge University Press

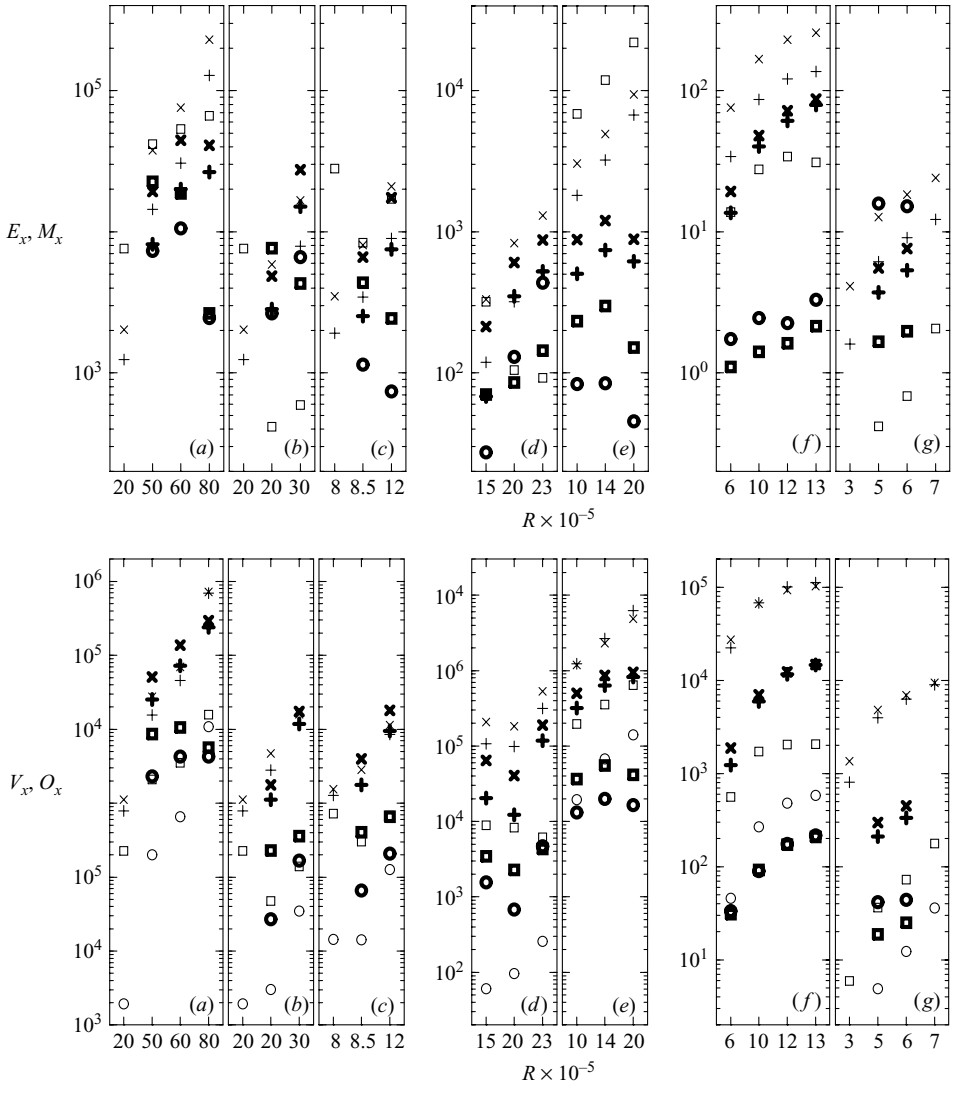


FIGURE 14. Kinetic E_x and magnetic M_x energy densities (upper row) and viscous V_x and Ohmic O_x dissipations (lower row) as functions of R for convection-driven dynamos in the cases (*a*) $P=0.1$, $\tau=10^5$, $P_m=0.2$, $\Lambda=0.38$; (*b*) $P=0.1$, $\tau=10^5$, $P_m=3$, $\Lambda=3.22$; (*c*) $P=0.1$, $\tau=3\times10^4$, $P_m=1$, $\Lambda=1.87$; (*d*) $P=1$, $\tau=3\times10^4$, $P_m=2$, $\Lambda=0.26$; (*e*) $P=1$, $\tau=5\times10^3$, $P_m=1$, $\Lambda=0.93$; (*f*) $P=5$, $\tau=5\times10^3$, $P_m=10$, $\Lambda=0.68$ and (*g*) $P=10$, $\tau=5\times10^3$, $P_m=10$, $\Lambda=0.12$. The components $\overline{X}_p$, $\overline{X}_t$, $\tilde{X}_p$, $\tilde{X}_t$ (where $X=E$, M, V, O) are represented by circles, squares, plus-signs and crosses, respectively. Kinetic energy densities and viscous dissipations are shown with light symbols, magnetic energy densities and ohmic dissipations are shown with heavy symbols. In case (*b*), results for a convection-driven dynamo, as well as for convection without magnetic field, have been plotted in the case $R=2\times10^6$. The values of Λ represent the highest values for each of the boxes.

begins to dominate. For dipolar dynamos obtained for $P=0.01$, $\tau=10^5$ with Rayleigh numbers of the order 10^6 and $0.2\leqslant P_m\leqslant0.5$, the energy of the mean toroidal field exceeds that of the mean poloidal field by more than a factor 10^2. For example, in the case $R=10^6$, $P_m=0.5$ the time-averaged magnetic energy densities $\overline{M}_p=146$ and

https://doi.org/10.1017/S0022112005004398 Published online by Cambridge University Press

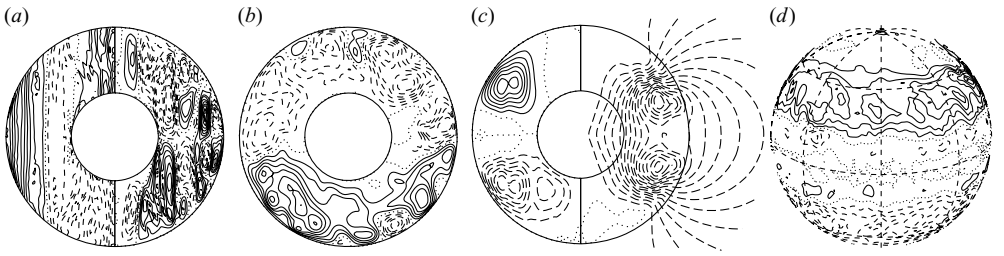


FIGURE 15. Convection-driven dynamo for $P=0.01$, $\tau=10^5$, $R=6\times10^5$ and $P_m=0.5$. (*a*) Lines of constant $\overline{u}_\varphi$ in the left half and streamlines, $r\sin\theta\partial_\theta\overline{v}=$ const. in the right half. (*b*) Streamlines in the equatorial plane, $r\partial_\varphi v=$ const. (*c*) The left half shows lines of constant zonal magnetic field $\overline{B}_\varphi$ and the right half shows meridional field lines, $r\sin\theta\partial_\theta\overline{h}=$ const. (*d*) Lines of constant B_r at the surface $r=r_o+0.5$.

$\overline{M}_t=2.26\times10^4$ are found. The structure of velocity and magnetic fields in this case is apparent from figure 15. The axisymmetric components of the magnetic field are almost steady in time; but the differential rotation in the polar regions may change its sign. At the particular time of figure 15, the zonal flows near the north and south poles have opposite signs. The fluctuating component of convection is dominated by the $(m=1)$-mode and exhibits the attachment to the equatorial boundary as must be expected for inertial convection according to the discussion in § 3. For Prandtl numbers of order 5 and higher, on the other hand, the energy of the mean poloidal field always exceeds that of the mean toroidal field, since the differential rotation which creates the latter is not strong enough. However, this changeover is gradual and depends more on the Rayleigh number than the other changeover discussed above.

Since in some of the cases of figure 14 the kinetic energies of convection in the absence of a magnetic field are shown, the effect of the magnetic field on convection becomes evident. In particular, in the cases with P of order unity or less, the energy of the mean toroidal velocity field is strongly reduced by the dynamo action in that the Lorentz force leads to a braking of the differential rotation as has been discussed by Grote & Busse (2001). On the other hand, the fluctuating components of convection are enhanced since the magnetic field prevents the onset of relaxation oscillations in which convection occurs only intermittently, as has been discussed in connection with figure 2. This effect is clearly demonstrated in case (*b*) of figure 14 where the results for convection with and without magnetic field are compared for $R=2\times10^6$. The same features are also revealed in figure 16 where a more general comparison between convection with and without magnetic fields is shown. This figure also demonstrates that the symmetry of the magnetic field does not play a major role in the considerations of energetic aspects of dynamos.

For Prandtl numbers larger than unity, the effect of the magnetic field is much reduced which is evident from the fact that the increasing magnetic energy for increasing P_m does not change the energy of the fluctuating components of convection, as can be seen in figure 13. Only the differential rotation is reduced through the strengthening of the Lorentz force. The diminished influence of magnetic field on convection is also evident from the property that typically viscous dissipation far exceeds ohmic dissipation for values of P of order 5 or higher, while the two sinks of energy are more comparable at low values of P.

https://doi.org/10.1017/S0022112005004398 Published online by Cambridge University Press

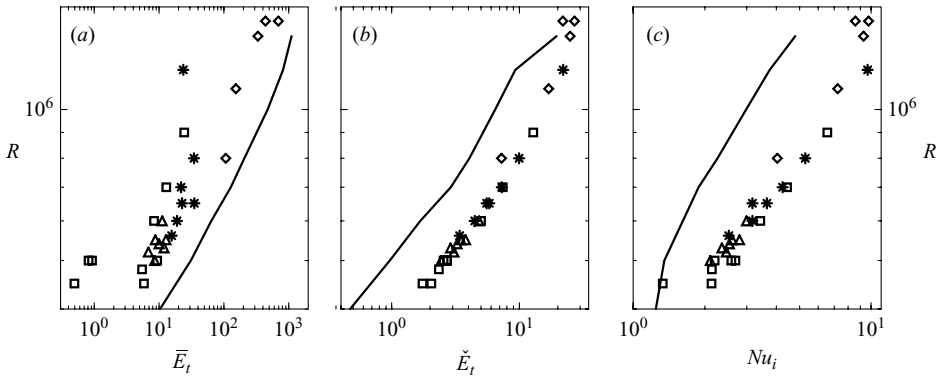


FIGURE 16. Time-averaged kinetic energy densities and Nusselt number Nu_i of non-magnetic convection (thick lines) and of quadrupolar (diamonds), mixed (stars), hemispherical (triangles) and chaotic dipolar dynamos (squares). Both non-magnetic convection and dynamo solutions are in the case $P=1$ and $\tau=10^4$. Values of P_m of the dynamo cases decrease from 10 to 0.4 as R increases. The densities $\overline{E}_t$, $\check{E}_t$ and Nu_i are shown in (*a*), (*b*) and (*c*), respectively.

6. Validity of the magnetostrophic approximation

Because convection-driven dynamos in rotating systems depend on a large number of parameters, it is desirable to eliminate one or more parameters through reductions of the basic equations. Among the nonlinear advection terms, the momentum advection term appears to be most expendable since it does not seem to be essential for convection-driven dynamos. In this way, the magnetostrophic approximation is obtained in which the acceleration of fluid particles is neglected in comparison to the Coriolis force and the Lorentz force. In general, this approximation can be obtained easily through the replacement of the viscous time scale d^2/ν by the time scale $d^2/(\kappa^{1-\gamma}\lambda^{\gamma})$ with $0\leqslant\gamma\leqslant1$ which is intermediate between the thermal and magnetic diffusion time scales. When $\sqrt{\rho\mu\kappa^{1-\gamma}\lambda^{\gamma}\nu}/d$ is used as the scale of the magnetic field, the basic dimensionless equations of motion, equation of induction and the heat equation can be written in the form

$$\left(P^{1-\gamma}P_m^{\gamma}\right)^{-1}(\partial_t\boldsymbol{u}+\boldsymbol{u}\cdot\nabla\boldsymbol{u})+\tau\boldsymbol{k}\times\boldsymbol{u}=-\nabla\pi+\Theta\boldsymbol{r}+\nabla^2\boldsymbol{u}+(\nabla\times\boldsymbol{B})\times\boldsymbol{B}, \quad (6.1a)$$

$$(P_m/P)^{\gamma}\,(\partial_t\boldsymbol{B}+\boldsymbol{u}\cdot\nabla\boldsymbol{B}-\boldsymbol{B}\cdot\nabla\boldsymbol{u})=\nabla^2\boldsymbol{B}, \quad (6.1b)$$

$$(P/P_m)^{1-\gamma}\,(\partial_t\Theta+\boldsymbol{u}\cdot\nabla\Theta)=R\boldsymbol{u}\cdot\boldsymbol{r}+\nabla^2\Theta, \quad (6.1c)$$

where $\boldsymbol{k}$ is the unit vector parallel to the axis of rotation. From the form of (6.1), it is clear that the magnetostrophic approximation should certainly be valid in the limit $P^{1-\gamma}P_m^{\gamma}\longrightarrow\infty$. In the following, we shall focus on the case $\gamma=0$. In figure 17, the energy densities have been plotted for fixed values of R,τ and of κ/λ. Since the fluctuating poloidal energy density $\check{E}_p$ always amounts to about 50 % of the corresponding toroidal one, it has not been plotted. It can be seen that the kinetic energies tend to become independent of P with increasing P in accordance with the magnetostrophic assumption. The energy density $\overline{E}_t$ representing the differential rotation is the only exception as expected. Little indication of an approach towards the validity of the magnetostrophic approximation is found, however, when the magnetic energy densities are considered. As has already been mentioned, the dynamo process is sensitive to the presence of the differential rotation, and much higher values of P may be needed before the magnetostrophic regime is approached. It is remarkable

https://doi.org/10.1017/S0022112005004398 Published online by Cambridge University Press

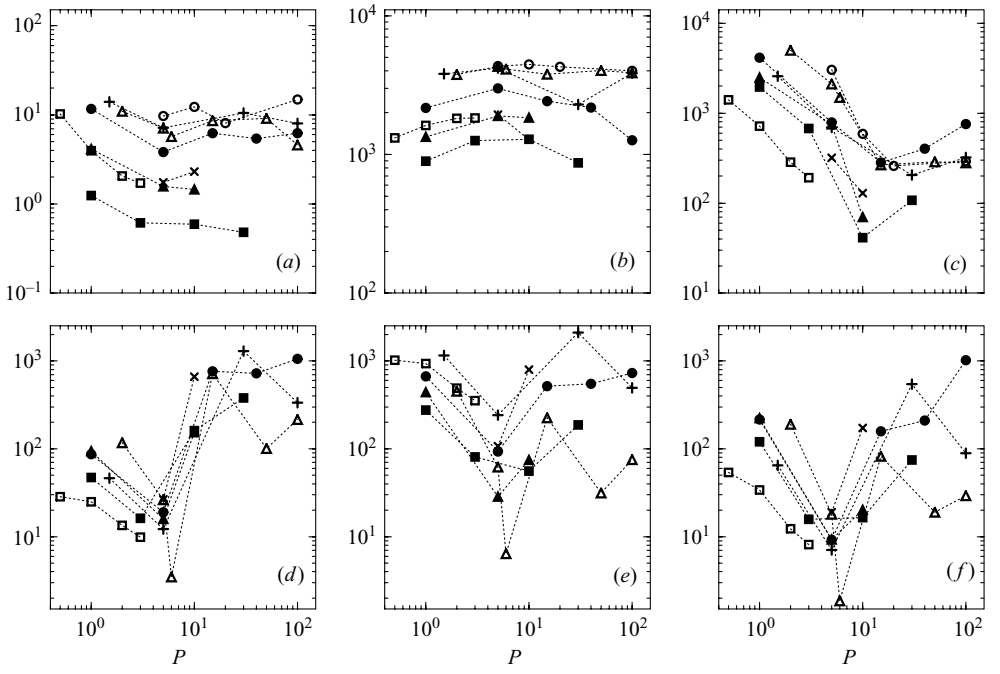


FIGURE 17. Kinetic energy densities (*a*) $\overline{E}_p$, (*b*) $\check{E}_t$ and (*c*) $\overline{E}_t$, all multiplied by P^2 as functions of P in the case $\tau = 5 \times 10^3$. The dynamos corresponding to $\kappa/\lambda = 1$, $R = 5 \times 10^5$ are indicated by solid squares, to $\kappa/\lambda = 1$, $R = 6 \times 10^5$ by solid triangles, to $\kappa/\lambda = 1$, $R = 8 \times 10^5$ by solid circles, to $\kappa/\lambda = 2$, $R = 6 \times 10^5$ by crosses, to $\kappa/\lambda = 2$, $R = 10^6$ by plus-signs, to $\kappa/\lambda = 5$, $R = 6 \times 10^5$ by open squares, to $\kappa/\lambda = 0.5$, $R = 10^6$ by open triangles and to non-magnetic convection with $R = 10^6$ by open circles. The second row shows the corresponding magnetic energy densities multiplied by P.

to see the distinct minimum of magnetic energies near $P = 8$ which corresponds to change in the structure of the magnetic field, as has been mentioned. The transition from a geostrophic differential rotation to a thermal wind one appears to be mainly responsible for this feature.

Results obtained on the basis of the magnetostrophic approximation in the case $\gamma = 0$ are by definition independent of P. In particular, the ratio between the magnetic energy and kinetic energy will be proportional to P (Glatzmaier & Roberts 1995) as is evident from the different scales used for the velocity and for $\boldsymbol{B}/\sqrt{\rho\mu}$ in (6.1*a*). The ratio between ohmic and viscous dissipation would be independent of P and would depend only on κ/λ. This latter parameter seems to be even more important than the magnetic Prandtl number for convection-driven dynamos. At least for Prandtl number of order unity or less, the condition $1 \lesssim P_m/P$ appears to apply for the minimum value P_m for which dynamo action can be obtained as is indicated by a comparison of dynamos obtained for $P = 1$ (see figure 1 of Grote, Busse & Tilgner 2000) and for $P = 0.1$ (see figure 9).

Similar conclusions to those reached for $\gamma = 0$ may be reached for $\gamma = 1$. In this case, the energy densities of figure 17 can be plotted as a function of P_m. For the cases $\kappa/\lambda = 1$, the plots remain unchanged with P_m replacing P at the abscissa. For other values of κ/λ, the respective data would just be shifted. Since no particular new insight appears to be evident, we have not included such a figure. The general conclusion to be drawn is that the magnetostrophic approximation

https://doi.org/10.1017/S0022112005004398 Published online by Cambridge University Press

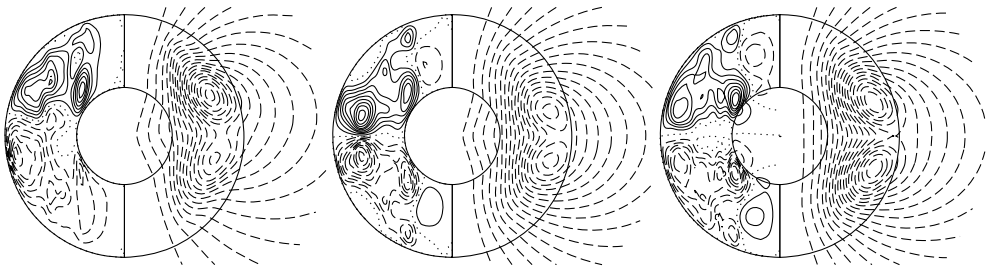


FIGURE 18. Effects of various boundary conditions on dynamo solutions for $P=0.1$, $\tau=10^5$, $R=4\times10^6$, $P_m=0.5$ in the dipolar cases **A**, **B**, **C** (from left to right) of table 1. The left halves of each plot show lines of constant zonal magnetic field $\overline{B}_\varphi$ and the right halves show meridional field lines, $r\sin\theta\partial_\theta\overline{h}=$ const., at particular moments in time.

seems to become valid only for fairly high values of the parameter $P^{1-\gamma}P_m^{\gamma}$ with $0\leqslant\gamma\leqslant1$. It should also be remembered that properties such as inertial convection and geostrophic differential rotation generated by Reynolds stresses disappear when the magnetostrophic approximation is used. Kuang & Bloxham (1997) have introduced for this reason a compromise in that the magnetostrophic approximation is applied only to the non-axisymmetric part of the equations of motion; but their main result that the ratio of magnetic to kinetic energy reaches 10^3 for $P=1$ is far removed from properties of other convection-driven spherical dynamos described in the literature.

7. Effects of boundary conditions on dynamo solutions

Because published solutions of convection-driven dynamos in rotating spherical shells are based on a variety of parameter values and satisfy different mechanical, thermal and magnetic boundary conditions, a systematic comparison between various models is difficult to conduct. An attempt to investigate the differences between numerical models based on various assumptions has most recently been made by Kutzner & Christensen (2000, 2002) who consider thermal and compositional driving with internal or external distribution of energy sources and a variety of thermal boundary conditions. Here we complement their studies with a few remarks on the possible effects of various velocity and magnetic boundary conditions. For this purpose, we have selected two typical dynamo solutions. The dynamo at parameter values $P=0.1$, $\tau=10^5$, $R=4\times10^6$, $P_m=0.5$ has a dipolar symmetry whereas the solution at $P=5$, $\tau=5\times10^3$, $R=8\times10^5$, $P_m=3$ has a quadrupolar one. We have repeated the simulations of these two cases for three of models with different combinations of boundary conditions and present the results in table 1. The results for the standard boundary conditions (2.7) and (2.8) used in this paper are listed under **A**. For type **B**, no-slip and insulating conditions have been adopted, for type **C** we have chosen no-slip conditions and a finitely conducting inner core and finally, type **D** has stress-free velocity boundary conditions and a perfectly conducting inner core. Thermal conditions have remained unchanged in that temperatures are fixed at the boundaries in all four models. Snapshots of the spatial structure of the magnetic field are shown in figures 18 and 19.

The replacement of the stress-free condition by the no-slip condition at the inner and outer boundaries leads to considerable changes in the structure of the velocity field which are even more dramatic in the absence of a magnetic field. The differential rotation is strongly inhibited by the Ekman layers which tend to oppose any deviation

https://doi.org/10.1017/S0022112005004398 Published online by Cambridge University Press

	$P=0.1,\ \tau=10^5,\ R=4\times10^6,\ P_m=0.5$					$P=5,\ \tau=5\times10^3,\ R=8\times10^5,\ P_m=3$			
	A	**B**	**B**	**C**	**D**	**A**	**B**	**C**	**D**
Type	D	D	–	D	Q	Q	–	–	Q
$\overline{E}_p$	0.286×10^2	0.112×10^2	0.939×10^2	0.108×10^2	0.299×10^2	0.157	0.611	0.523	0.147
$\overline{E}_t$	0.599×10^4	0.647×10^3	0.757×10^5	0.807×10^3	0.764×10^4	0.533×10^2	0.105×10^2	0.106×10^2	0.528×10^2
$\check{E}_p$	0.142×10^5	0.115×10^5	0.221×10^5	0.121×10^5	0.138×10^5	0.574×10^2	0.614×10^2	0.611×10^2	0.566×10^2
$\check{E}_t$	0.336×10^5	0.257×10^5	0.540×10^5	0.273×10^5	0.247×10^5	0.119×10^3	0.983×10^2	0.952×10^2	0.119×10^3
$\overline{M}_p$	0.129×10^5	0.392×10^5	–	0.355×10^5	0.768×10^3	0.487×10	–	–	0.466×10
$\overline{M}_t$	0.133×10^5	0.879×10^4	–	0.716×10^4	0.538×10^5	0.325×10	–	–	0.336×10
$\check{M}_p$	0.136×10^5	0.169×10^5	–	0.147×10^5	0.148×10^5	0.818×10	–	–	0.837×10
$\check{M}_t$	0.307×10^5	0.345×10^5	–	0.327×10^5	0.448×10^4	0.109×10^2	–	–	0.110×10^2
$\overline{V}_p$	0.643×10^5	0.104×10^6	0.107×10^8	0.122×10^6	0.462×10^5	0.151×10^3	0.111×10^4	0.686×10^3	0.140×10^3
$\overline{V}_t$	0.584×10^6	0.366×10^6	0.277×10^8	0.348×10^6	0.709×10^6	0.182×10^4	0.342×10^4	0.245×10^4	0.179×10^4
$\check{V}_p$	0.133×10^8	0.179×10^8	0.448×10^8	0.191×10^8	0.125×10^8	0.414×10^5	0.524×10^5	0.528×10^5	0.406×10^5
$\check{V}_t$	0.229×10^8	0.354×10^8	0.821×10^8	0.372×10^8	0.171×10^8	0.455×10^5	0.580×10^5	0.568×10^5	0.450×10^5
$\overline{O}_p$	0.626×10^6	0.129×10^7	–	0.120×10^7	0.874×10^5	0.544×10^3	–	–	0.520×10^3
$\overline{O}_t$	0.148×10^7	0.944×10^6	–	0.890×10^6	0.222×10^7	0.359×10^3	–	–	0.372×10^3
$\check{O}_p$	0.125×10^8	0.138×10^8	–	0.133×10^8	0.106×10^8	0.468×10^4	–	–	0.488×10^4
$\check{O}_t$	0.253×10^8	0.268×10^8	–	0.276×10^8	0.362×10^7	0.600×10^4	–	–	0.587×10^4
Λ	0.707	0.995	–	0.902	0.740	0.032	–	–	0.032
Rm	164	138	–	142	152	64	55	55	64
Nu_i	2.125	2.275	2.442	2.316	1.563	11.285	12.968	12.729	11.194

TABLE 1. Time-averaged global properties of dynamos with various velocity and magnetic boundary conditions as follows. **A**: stress-free and insulating, **B**: no-slip and insulating, **C**: no-slip and a finitely conducting inner core and **D**: stress-free and a perfectly conducting inner core. The predominant symmetry type is indicated with 'D' if dipolar, 'Q' if quadrupolar and '–' if the dynamo is decaying. In case **B** in the left-hand part of the table, results for both a dynamo solution and a non-magnetic convection case are given.

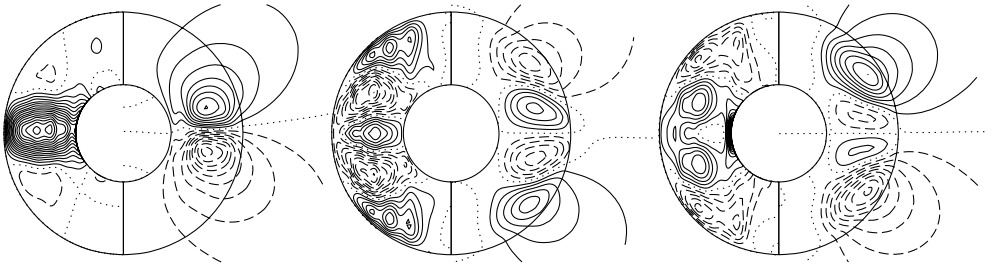


FIGURE 19. Same as figure 18 but for the quadrupolar case **D** for the parameter values $P=0.1$, $\tau=10^5$, $R=4\times10^6$, $P_m=0.5$ and cases **A** and **D** for the parameter values $P=5$, $\tau=5\times10^3$, $R=8\times10^5$, $P_m=3$.

from rigid-body rotation. The circulation induced by the Ekman layers, on the other hand, promotes the heat transport and is responsible for the fact that the energy component $\overline{E}_p$ is typically much larger in the case of no-slip boundaries than in the case of stress-free ones. However, the main effect of the rigid boundaries is the suppression of the destruction of convection columns by the shearing action of the differential rotation. Relaxation oscillations which are predominant for Prandtl numbers of order unity or less in the presence of stress-free conditions have not yet been found when no-slip conditions are used. It must be expected, however, that the

https://doi.org/10.1017/S0022112005004398 Published online by Cambridge University Press

properties of convection with rigid boundaries will approach those of convection with free boundaries as the Coriolis number τ increases and the influence of the Ekman layer decreases.

The effects caused by the differences in the velocity boundary conditions are reduced in the presence of a magnetic field generated by the dynamo process. The differential rotation is reduced by the action of the Lorentz force for both types of boundary conditions; but while the energy of the fluctuating components of convection is amplified by the presence of the magnetic field this effect usually does not happen in the case of no-slip boundaries as is evident from case **B** of table 1. On the contrary, the magnetic degrees of freedom compete with kinetic ones for the same source of energy. Nevertheless, in spite of the lower kinetic energies in case **B** in comparison to those of case **A**, case **B** still exhibits a higher convective heat transport as is evident from the Nusselt number.

The comparison of convection-driven dynamos in case of $P = 5$ as presented by the right-hand side of table 1 has been less successful since it was not possible to obtain dynamos in the cases **B** and **D** even after the Rayleigh number has been increased up to twice the indicated value. Except for the axisymmetric components of the velocities, the kinetic energies of the cases **A** and **B** are surprisingly close, which indicates that the effect of no-slip boundaries on convection is similar to that of a dynamo-generated magnetic field. The closeness of the energy results of the cases **A** and **D** for both values of P and of cases **B** and **C** for $P = 0.1$ indicates that the magnetic boundary conditions at the inner core have little influence on the dynamo process. It is remarkable, however, that in case **D** a quadrupolar dynamo is realized instead of the dipolar one in the standard case **A**. Even more remarkable is the property that this quadrupolar dynamo does not oscillate in time as has been found for all quadrupolar dynamos with the boundary conditions (2.8). From a general point of view, it must be expected that for turbulent dynamos, the inner core cannot exert a strong influence on the dynamo process since the highly fluctuating magnetic field will not penetrate far into the inner core nor is it likely that strong fluxes will accumulate there since they are subject to ohmic decay. Wicht (2002) has arrived at similar conclusions.

8. Concluding remarks

In this paper, the analysis of convection-driven dynamos has focused on the Prandtl-number dependence while other parameters such as R and τ have not been varied as much, but instead have been kept at reasonably high values which are numerically accessible with adequate resolution in space and in time. In the case of the Rayleigh number, the numerical limitations are not felt as strongly as in the case of τ, since dynamos often seem to disappear, or at least exhibit decreasing energies of the axisymmetric components of their magnetic fields, as R is increased beyond an optimal value. More restrictive are the limits on the Coriolis number τ which have prevented so far the attainment of dynamos dominated by ohmic dissipation. While the latter exceeds the viscous dissipation in some of the low-Prandtl-number dynamos, sufficient viscous friction always seems to be required to obtain numerically well-behaved solutions. Ohmic dissipation also helps in this respect and permits solutions at values of R and τ which are not accessible at the same numerical resolution without magnetic field; but ohmic dissipation does not necessarily prevent tangential discontinuities of the velocity field which are possible in the absence of viscous friction.

https://doi.org/10.1017/S0022112005004398 Published online by Cambridge University Press

A primary goal of dynamo simulations are results which can be compared quantitatively with properties of the geomagnetic field and its variations in time. The geodynamo appears to exhibit features which are similar to those of convection-driven dynamos with large values of P as well as to those with P of the order of unity. The fact that the magnetic energy exceeds the kinetic energy in the Earth's core by a factor of order 10^3 together with the property that the axisymmetric poloidal component of the geomagnetic field dominates over the non-axisymmetric components suggests that the geodynamo resembles a high-P dynamo. On the other hand, the strong variations of the amplitude of the magnetic field on the magnetic diffusion time scale together with the torsional oscillations which manifest themselves as 'jerks' on a much shorter time scale (Bloxham, Zatman & Dumberry 2002) indicates a relationship to dynamos with $P \lesssim 1$ (Busse & Simitev 2005). Of course, these similarities may change when more realistic dynamo simulations with much lower values of the magnetic Prandtl number P_m become possible; but they could also indicate that the two sources of buoyancy apparently present in the Earth's core – the thermal one characterized by $P < 1$ and the compositional one characterized by $P \gg 1$ – should be distinguished in dynamo simulations. An indication that new dynamical effects become important in the presence of buoyancy sources with rather different diffusivities has been given by the linear analysis of Busse (2002*b*).

The research reported in this paper has been supported by the *Deutsche Forschungsgemeinschaft* under Grants Bu589/10-1,2. The computer time provided by the *Höchstleistungsrechenzentrum Stuttgart* is also gratefully acknowledged.

REFERENCES

Ahlers, G. & Xu, X. 2001 Prandtl number dependence of heat transport in turbulent Rayleigh–Bénard convection. *Phys. Rev. Lett.* **86**, 3320–3323.

Ardes, M., Busse, F. H. & Wicht, J. 1997 Thermal convection in rotating spherical shell. *Phys. Earth Planet. Inter.* **99**, 55–67.

Bloxham, J., Zatman, S. & Dumberry, M. 2002 The origin of geomagnetic jerks. *Nature* **240**, 65–68.

Braginsky, S. I. & Roberts, P. H. 1995 Equations governing convection in Earth's core and the geodynamo. *Geophys. Astrophys. Fluid Dyn.* **79**, 1–97.

Busse, F. H. 2002*a* Convection flows in rapidly rotating spheres and their dynamo action. *Phys. Fluids* **14**, 1301–1314.

Busse, F. H. 2002*b* Is low Rayleigh number convection possible in the Earth's core? *Geophys. Res. Lett.* **29**, GLO149597.

Busse, F. H. & Cuong, P. G. 1977 Convection in rapidly rotating spherical fluid shells. *Geophys. Astrophys. Fluid Dyn.* **8**, 17–41.

Busse, F. H., Grote, E. & Simitev, R. 2003 Convection in rotating spherical shells and its dynamo action. In *Earth's Core and Lower Mantle* (ed. C. A. Jones, A. M. Soward & K. Zhang) pp. 130–152. Taylor & Francis.

Busse, F. H., Grote, E. & Tilgner, A. 1998 On convection driven dynamos in rotating spherical shells. *Studia Geoph. Geod.* **42**, 211–223.

Busse, F. H. & Simitev, R. 2004 Inertial convection in rotating fluid spheres. *J. Fluid Mech.* **498**, 23–30.

Busse, F. H. & Simitev, R. 2005 Convection in rotating spherical fluid shells and its dynamo states. In *Fluid Dynamics and Dynamos in Astrophysics and Geophysics* (ed. A. M. Soward, C. A. Jones, D. W. Hughes & N. O. Weiss), pp. 359–392. Taylor & Francis.

Chandrasekhar, S. 1961 *Hydrodynamic and Hydromagnetic Stability*. Clarendon.

Christensen, U., Olson, P. & Glatzmaier, G. A. 1999 Numerical modeling of the geodynamo: a systematic parameter study. *Geophys. J. Intl* **138**, 393–409.

Eschrich, K.-O. & Rüdiger, G. 1983 A second-order correlation approximation for thermal conductivity and Prandtl number of free turbulence. *Astron. Nachr.* **304**, 171–180.

https://doi.org/10.1017/S0022112005004398 Published online by Cambridge University Press

Glatzmaier, G. A. & Roberts, P. H. 1995 A three-dimensional convection dynamo solution with rotating and finitely conducting inner core and mantle. *Phys. Earth Planet. Inter.* **91**, 63–75.

Grote, E. & Busse, F. H. 2000 Hemispherical dynamos generated by convection in rotating spherical shells. *Phys. Rev.* E **62**, 4457–4460.

Grote, E. & Busse, F. H. 2001 Dynamics of convection and dynamos in rotating spherical fluid shells. *Fluid Dyn. Res.* **28**, 349–368.

Grote, E., Busse, F. H. & Simitev, R. 2001 Buoyancy driven convection in rotating spherical shells and its dynamo action. In *High Performance Computing in Science and Engineering '01* (ed. E. Krause & W. Jäger), pp. 12–34. Springer.

Grote, E., Busse, F. H. & Tilgner, A. 1999 Convection-driven quadrupolar dynamos in rotating spherical shells, *Phys. Rev.* E **60**, R5025–R5028.

Grote, E., Busse, F. H. & Tilgner, A. 2000 Regular and chaotic spherical dynamos. *Phys. Earth Planet. Inter.* **117**, 259–272.

Ishihara, N. & Kida, S. 2002 Dynamo mechanism in a rotating spherical shell: competition between magnetic field and convection vortices. *J. Fluid Mech.* **465**, 1–32.

Kageyama, A. & Sato, T. 1997 Generation mechanism of a dipole field by a magnetohydrodynamic dynamo. *Phys. Rev.* E **55**, 4617–4626.

Katayama, J. S., Matsushima, M. & Honkura, Y. 1999 Some characteristics of magnetic field behavior in a model of MHD dynamo thermally driven in a rotating spherical shell. *Phys. Earth Planet. Inter.* **111**, 141–159.

Kida, S. & Kitauchi, H. 1998 Thermally driven MHD dynamo in a rotating spherical shell. *Prog. Theor. Phys. Suppl.* **130**, 121–136.

Kuang, W. & Bloxham, J. 1997 An Earth-like numerical dynamo model. *Nature* **389**, 371–374.

Kutzner, C. & Christensen, U. R. 2000 Effects of driving mechanisms in geodynamo models. *Geophys. Res. Lett.* **27**, 29–32.

Kutzner, C. & Christensen, U. R. 2002 From stable dipolar towards reversing numerical dynamos. *Phys. Earth Planet. Inter.* **131**, 29–45.

Olson, P., Christensen, U. & Glatzmaier, G. A. 1999 Numerical modeling of the geodynamo: mechanism of field generation and equilibration. *J. Geophys. Res.* **104**, 10 383–10 404.

Simitev, R. & Busse, F. H. 2003 Patterns of convection in rotating spherical shells. *New J. Phys.* **5**, 97.1–97.20.

Takahashi, F., Matsushima, M. & Honkura, Y. 2003 Dynamo action and its temporal variation inside the tangent cylinder in MHD dynamo simulations. *Phys. Earth Planet. Inter.* **140**, 53–71.

Tilgner, A. & Busse, F. H. 1997 Finite amplitude convection in rotating spherical fluid shells. *J. Fluid Mech.* **332**, 359–376.

Wicht, J. 2002 Inner-core conductivity in numerical dynamo simulations. *Phys. Earth Planet. Inter.* **132**, 281–302.

Zhang, K. 1994 On coupling between the Poincaré equation and the heat equation. *J. Fluid Mech.* **268**, 211–229.

Zhang, K. 1995 On coupling between the Poincaré equation and the heat equation: no-slip boundary condition. *J. Fluid Mech.* **284**, 239–256.

Zhang, K. & Busse, F. H. 1987 On the onset of convection in rotating spherical shells. *Geophys. Astrophys. Fluid Dyn.* **39**, 119–147.

Zhang, K. & Busse, F. H. 1989 Convection driven magnetohydrodynamic dynamos in rotating spherical shells. *Geophys. Astrophys. Fluid Dyn.* **49**, 97–116.

Zhang, K. & Busse, F. H. 1990 Generation of magnetic field by convection in a rotating spherical fluid shell of infinite Prandtl number. *Phys. Earth Planet. Inter.* **59**, 208–222.

https://doi.org/10.1017/S0022112005004398 Published online by Cambridge University Press